Cement and Concrete Research 39 (2009) 687–695

Contents lists available at ScienceDirect

Cement and Concrete Research

journal homepage: http://ees.elsevier.com/CEMCON/default.asp

# Characterization of concrete properties from dielectric properties using ground penetrating radar

W.L. Lai [a], S.C. Kou [a], W.F. Tsang [b], C.S. Poon [a,*]

[a] Department of Civil and Structural Engineering, The Hong Kong Polytechnic University, Hung Hom, Kowloon, Hong Kong
[b] Department of Building and Real Estate, The Hong Kong Polytechnic University, Hung Hom, Kowloon, Hong Kong

ARTICLE INFO

*Article history:*
Received 3 August 2007
Accepted 14 May 2009

*Keywords:*
Lightweight and normal aggregate concrete
Ground penetrating radar
Real permittivity
Wave energy level
Free water
Absorbed/bound water

ABSTRACT

This paper presents the experimental results of a study of the relationships between light-weight (LWAC) and normal aggregate concrete (NAC) properties, as well as radar wave properties that are derived by using ground penetrating radar (GPR). The former (LWAC) refers to compressive strength, apparent porosity and saturated density, while the latter (NAC) refers to real part of dielectric permittivity ($\varepsilon'$ or real permittivity) and wave energy level ($E$). Throughout the test period of the newly cast concrete cured for 90 days, the above mentioned material properties gradually changed which can be attributed to the effects of cement hydration, different types of aggregates and initial water to binder ratios. A number of plots describing various properties of concrete such as dielectric, strength and porosity perspectives were established. From these plots, we compare the characteristics of how much and how fast free water was turned to absorbed water in LWAC and NAC. The underlying mechanisms and a mechanistic model are then developed.

## 1. Introduction

Developments of nondestructive testing methods in civil engineering applications are growing rapidly [1,2]. Ground penetrating radar (GPR), as one of the most promising nondestructive testing techniques, has been widely accepted as an effective means to 'see through' concrete structures, such as dams [3] and bridges [4]. Fundamental principles of using GPR to solve a variety of civil engineering problems have been widely documented [2,5,6]; whilst an excellent review of the recent application of GPR in civil engineering has been given by [1]. Most of the published work in this regard concentrated on locating and characterizing anomalies (such as reinforcement and voids) embedded in concrete. But little effort seems to have been expended to investigate the relationships between dielectric properties (using GPR), as well as other mechanical and physical properties such as strength of concrete [7], asphalt [8]; and soil [9]. As far as concrete is concerned, a few researchers have looked into the effect of the degree of hydration of a small and localized volume of concrete on the dielectric properties using either a microwave terminal [10,11] or a dielectric sensor [12]. Larger scale investigations using GPR have been used to assess concrete composition [13], moisture contents [14,15] and pore size distribution [16].

This paper attempts to characterize concrete properties in terms of dielectric properties. The aims are: (1) the mechanism of transformation of free to absorbed/bound water (physically absorbed/chemically bound water) during the cement hydration process through measuring $\varepsilon'$, (2) different $\varepsilon'$ signatures for LWAC and NAC during the hydration process, (3) relationships amongst $\varepsilon'$, $E$ and compressive strength at the same age, and (4) the effects of water to binder ($W/B$) ratios on $\varepsilon'$. The first two focuses are solely from dielectric perspectives, whilst the latter two study dielectric, as well as mechanical and physical properties of concrete jointly. The paper can be regarded as an extension of the authors' other paper [17], which studied the water-exchange process in light-weight and normal aggregate concretes from freshly mixed to the first 48 h after mixing.

## 2. Theoretical background

Factors influencing the dielectric properties of a material were summarized by [18] and re-interpreted in [19]. Presence of water is recognized as the primary and dominant factor surrounding the increase of $\varepsilon'$ in concrete [15,16,20]. Other influencing factors are:

(1) electromagnetic (EM) frequency [21–23],
(2) water to cement ratio [7,20],
(3) porosity [7,16]
(4) ions in pore solution which make the material behave as conducting dielectrics [6], and
(5) clay minerals of wide range of porosities and specific surfaces [24].

Factors such as cement type, salt impregnation, presence of pulverized fuel ash and ground granulated blast furnace slag, and

---

* Corresponding author.
*E-mail address:* cecspoon@inet.polyu.edu.hk (C.S. Poon).

0008-8846/$ – see front matter © 2009 Elsevier Ltd. All rights reserved.
doi:10.1016/j.cemconres.2009.05.004

**Table 1**
Properties of Portland cement and silica fume.

| Parameter | Cement | Silica fume |
|---|---|---|
| $SiO_2$ | 21.0 | 85–96 |
| $Al_2O_3$ | 5.9 | – |
| $Fe_2O_3$ | 3.4 | – |
| CaO | 64.7 | – |
| MgO | 0.9 | – |
| $Na_2O$ | – | – |
| $K_2O$ | – | – |
| $TiO_2$ | – | – |
| $SO_3$ | 2.6 | 0.3–0.7 |
| Loss on ignition (%) | 1.2 | 3.5 |
| Specific gravity (g/cm$^3$) | 3.15 | 2.22 |
| Fineness (>45 µm) | – | 3–5 |
| Specific surface (cm$^2$/g) | 3520 | – |

temperature during tests are reported to be of minor or negligible significance [20]. Literature was scarcely reported on the effects of different types of dense aggregate on ε'. However it is believed that the effects should be insignificant because of the relatively small variations of aggregate density.

During the hydration process, concrete changes from the fresh to the hardened state. During this process, free water is reduced, absorbed and bounded progressively because chemical reaction turns the water from the free to the bound form. In soil science, the differentiation of soil water between the completely free and the bound states can be defined by two intermediate states of wetness. The first state is termed *field capacity*. It is a measure of wetness when a soil was drained for about 2 days [25]. Beyond this field capacity boundary, water is free to flow by gravity. The second state is wilting point. When water gets absorbed by and gets closer to the soil particles, the wilting point is reached so that water becomes bounded. The evidence of the wilting point is attributed to the existence of monolayer(s) of absorbed water coated on the solid surface where the moisture content is low [26]. Based on these two water states, a model depicting successive layers of water surrounding a soil particle was established [27]. The model starts from the outer-most water layer (field capacity) to the intermediate water layer (wilting point), and then to the innermost mono-layer [27]. At the wilting point and the innermost mono-layer, water molecules are tightly bounded to the solid particles.

The above soil–water model can be used to interpret and understand the continuous change of dielectric properties of water from the conducting (free water) to the non-conducting (absorbed/bound water) states during the hydration process of cement in concrete. An exception of this interpretation is that the terminologies ‘field capacity’ and ‘wilting point’ are avoided because the porous media in concrete and soil are different in nature and scale. The polarization (due to an external EM field) of the absorbed/bound water layer in a cement paste's (transition point) (analogous to soil's wilting point) is limited since it is tightly bound to the solid surface [26]. Hence the contribution of the absorbed/bound water towards polarization is greatly reduced. This is contrary to the free water beyond the transition point, which enhances the overall polarization by allowing the formation of water–solid grain dielectric and water–gas grain dielectrics [28]. The transition from the free to the absorbed/bound form of water can be revealed by the changes of magnitude of polarization as measured by bulk ε'. This bulk ε' can be measurable by an electromagnetic coaxial transmission line [20], a cast-in dielectric probe [12], and GPR [8]. GPR is considered to be the most appropriate technology for this study, as it is entirely nondestructive and can be used to study the largest volume of materials.

## 3. Specimen preparation

ASTM Type I Portland cement and condensed silica fume (SF) (Force 10,000D microsilica) for LWAC were used in the concrete mixtures. The chemical and physical properties of cement and silica fume are given in Table 1. The constituents of the concrete mixes are in Table 2.

The light-weight aggregate (LWA) was a commercially available product. The main composition of the LWA was expanded clay. The nominal sizes of the aggregate were 18 mm and 5 mm. The water absorptions of these two sized aggregates at 24 h are 29% and 22% respectively; and the surface saturated densities are 1175 and 648 kg/m$^3$ respectively. In this study, crushed granite (with density 2650 kg/m$^3$) was used as the natural aggregate with nominal sizes of 20 and 10 mm and their particle size distributions conformed to [29]. Quartz river sand (with density 2620 kg/m$^3$ and water absorption 0.87% at 24 h) was used as the fine aggregate in the concrete mixtures.

For the LWAC and NAC concrete mixtures, a sulfonated naphthalene formaldehyde condensate was used as a superplasticizer. This superplasticizer is available as a dark-brown 40–42% solids aqueous solution with a density of 1210 kg/m$^3$. This chemical admixture was used to control the slump flow diameter of the fresh concrete mixes at 650 mm ± 25 mm. For each of the concrete specimens, 100 mm cubes, 200($L$) × 200($W$) × 150($H$) mm slabs, and 100 (dia.) × 50 ($H$) mm short

**Table 2**
Design specification of concrete specimens.

| Category[a] | Specimen reference | Bulk density (kg/ m$^3$) | | | | | | | | | Water to binder ($W/B$) ratio[d] | Oven-dry ensity at 28 days (kg/m$^3$) |
|---|---|---|---|---|---|---|---|---|---|---|---|---|
| | | Binder | | Superplasticizer | Water* | Fine aggregate | Coarse aggregate | | Water contained in light-weight aggregate** | Total free water[c] | | |
| | | Cement | Silica fume | | | | Light-weight[b] | Granite | | | | |
| Light-weight aggregate concrete (LWAC)[c] | LW35D | 436 | 35 | 4 | 163 | 635 | 430 | – | 113 | 276 | 0.35 | 1625 |
| | LW45D | 480 | 50 | 4.3 | 201 | 644 | 430 | – | 113 | 314 | 0.38 | 1714 |
| | LW65D-1 | 500 | 50 | 4.5 | 187 | 650 | 437 | – | 115 | 302 | 0.34 | 1798 |
| | LW65D-2 | 500 | 50 | 4.5 | 176 | 650 | 448 | – | 118 | 294 | 0.32 | 1724 |
| | LW85D | 600 | 60 | 5 | 185 | 452 | 483 | – | 127 | 312 | 0.28 | 1739 |
| Normal aggregate concrete (NAC) | N40D-1 | 335 | – | – | 190 | 680 | – | 1145 | – | 190 | 0.57 | 2289 |
| | N40D-2 | 295 | – | – | 192 | 757 | – | 1136 | – | 192 | 0.65 | N/A |
| | N55D | 375 | – | – | 191 | 671 | – | 1143 | – | 191 | 0.51 | N/A |
| | N75D | 400 | – | – | 190 | 634 | – | 1150 | – | 190 | 0.48 | 2298 |

Remarks:

[a] LWAC: light-weight aggregate concrete; NAC: normal aggregate concrete. The numbers between the letters indicate the strength reached at day 28 (abbreviated as ‘D’).

[b] Type of light-weight aggregate is Swedish Leca™. The aggregates were pre-soaked in water before mixing.

[c] Total free water means = (water* + water contained in light-weight aggregate**).

[d] The $W/B$ does not take into account the water contained initially in LWA which was pre-soaked in water before mixing.

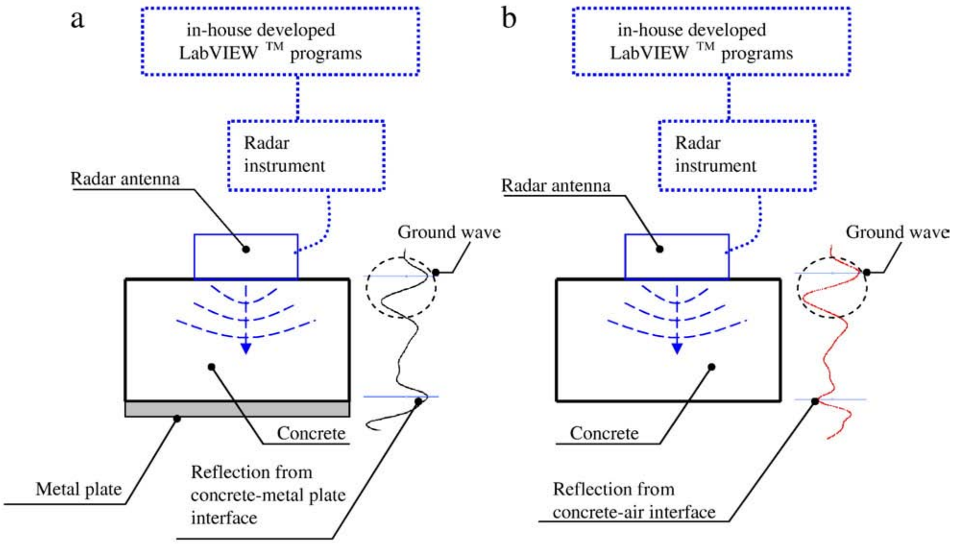

**Fig. 1.** a. Schematic representation of the experimental setup and associated waveforms obtained *with* a metal plate attached to the concrete soffit. b. Schematic representation of the experimental setup and associated waveforms obtained *without* a metal plate attached to the concrete soffit.

cylinders were cast. The cubes and slabs were used to determine the compressive strength and real permittivity ($\varepsilon'$)/wave energy level ($E$) respectively; while the cylinders were used to determine apparent porosity. The cube and cylindrical specimens were cast in steel moulds and compacted using a vibrating table; while the slab specimens were cast in a timber formwork and compacted using a tamping rod. The specimens were cured in a water-curing tank at 27 ± 1 °C until the age needed for testing. Specimens with very slight difference in mix proportions (LW65-1 and −2 or N40-1 and −2) were cast to test the repeatability of the casting and testing procedures.

## 4. Determination of real permittivity, wave energy level, compressive strength and apparent porosity

The GPR system adopted in these experiments was a JEJ-60BF (manufactured by Japan Radio Company Limited) mono-static radar system equipped with a 1 GHz antenna. The data acquisition and processing units of the 1 GHz antenna were assembled by 'National Instrument™' hardware and a software program developed in-house which was established in the 'LabVIEW™' environment, as shown in Fig. 1a and b. The LabVIEW program performed a series of automated data acquisition and signal processing tasks [19]; as well as data analysis which determined the real permittivity and wave energy levels.

### 4.1. Real permittivity ($\varepsilon'$)

The bulk $\varepsilon'$ of the concrete specimens at different curing ages were determined by using the waveforms obtained by the GPR system via the following steps: (1) recognizing the local positive and negative maximum reflections in the waveforms captured with (Figs. 1a and 2) and without (Figs. 1b and 2) the metal plate attached to the concrete soffit respectively; (2) subtracting the waveforms captured without the metal plate from those with the metal plate, as illustrated in Fig. 3, so that the first peaks corresponding to the concrete soffit can be clearly identified; (3) determining the two-way-transit-time ($T$) required to travel back and forth from the antenna (i.e. the specimen

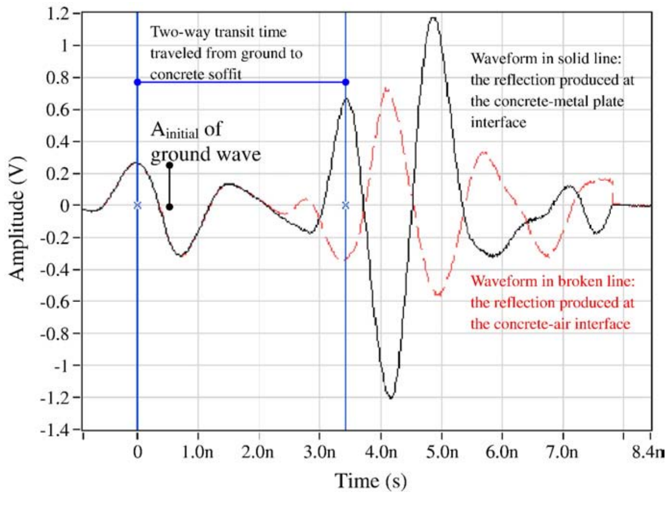

**Fig. 2.** Overlaid waveforms obtained from Fig. 1a and b.

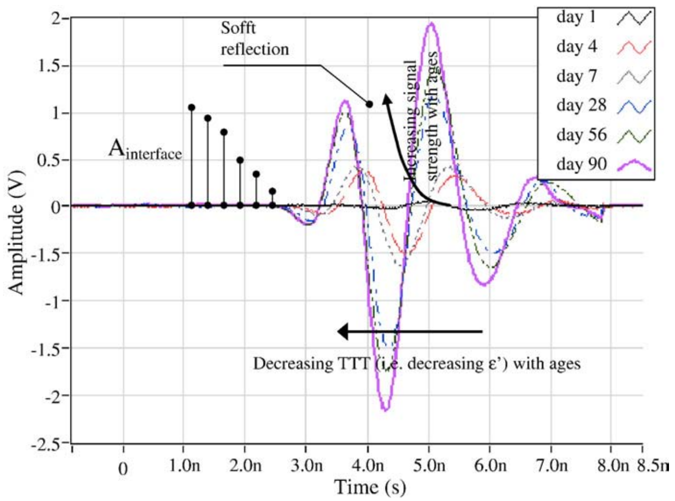

**Fig. 3.** Results of waveform subtractions of concrete–air interface from concrete–steel plate in LW45D at various ages.

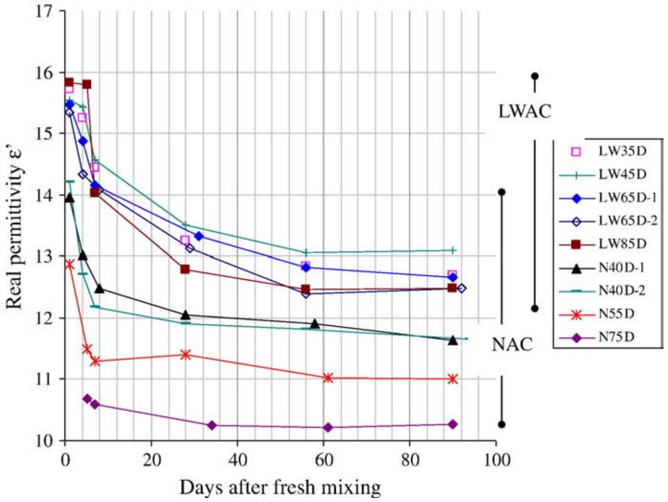

**Fig. 4.** Reduction of real permittivity with age.

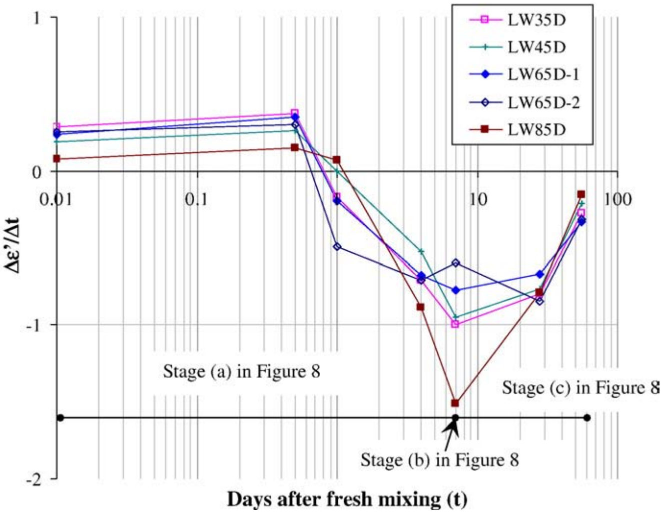

**Fig. 6.** Rate of change of real permittivity for LWAC.

surface) to the concrete soffit; and (4) computing ε' according to Eq. (1) [30,31].

$$v = \frac{2D}{T} = \frac{c}{\sqrt{\varepsilon'}} \qquad (1)$$

where $v$ = radar wave velocity (m/s), $D$ = thickness of specimens, $T$ = radar wave traveling time (s), $c$ = speed of light (m/s) and $\varepsilon'$ = real part of dielectric permittivity.

### 4.2. Wave energy levels (E)

Wave energy level represents the EM energy absorbed by the specimens at various ages. It was measured by subtracting the waveforms acquired from the concrete soffit by those from the metal plate, as mentioned above and shown in Fig. 1. The results can be found in Fig. 3. The wave energy levels are quantified by measuring the increase of signal amplitudes of the first peaks corresponding to the concrete soffit. The signal amplitudes (i.e. measured by volts) at these first peaks are normalized and expressed in a dB/m scale. With this normalized scale, the amplitudes of the first arrival reflections are divided by those of the ground wave (i.e. $A_{\text{initial}}$), as shown in Fig. 2 and according to Eq. (2) [16].

$$\text{Wave energy level } (E) \text{ expressed in dB/m} = \left(20 \times \log\frac{A_{\text{reflection}}}{A_{\text{initial}}}\right) / D \qquad (2)$$

where $A_{\text{reflection}}$ = amplitude of the material interface, $A_{\text{initial}}$ = amplitude of reflection of the initial peak (refer to Fig. 2), $D$ = the thickness of the specimen.

### 4.3. Compressive strength

The compressive strengths of concrete were determined according to [32] and with a Denison compression machine which offers a loading capacity of 3000 kN and loading rate 200 kN/min. The compressive strengths of each of the mixes were measured on the 100 mm cubes at the ages of 1, 4, 7, 28, 56 and 90 days. The reported values are the average values of three cubes.

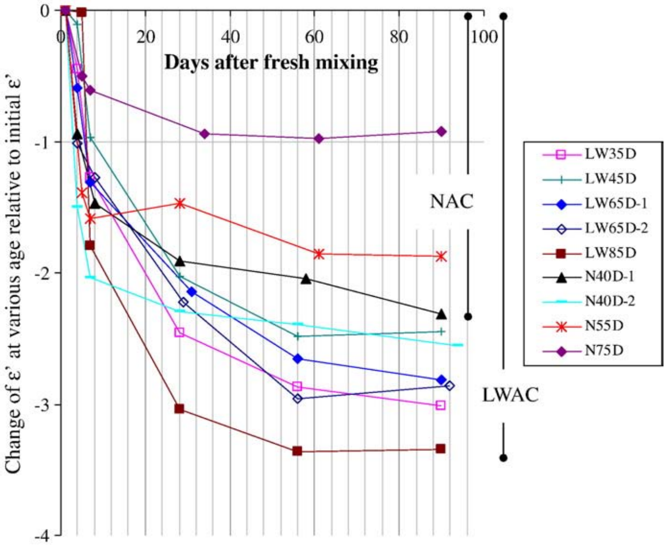

**Fig. 5.** Change of real permittivity for LWAC and NAC with respect to initial real permittivity.

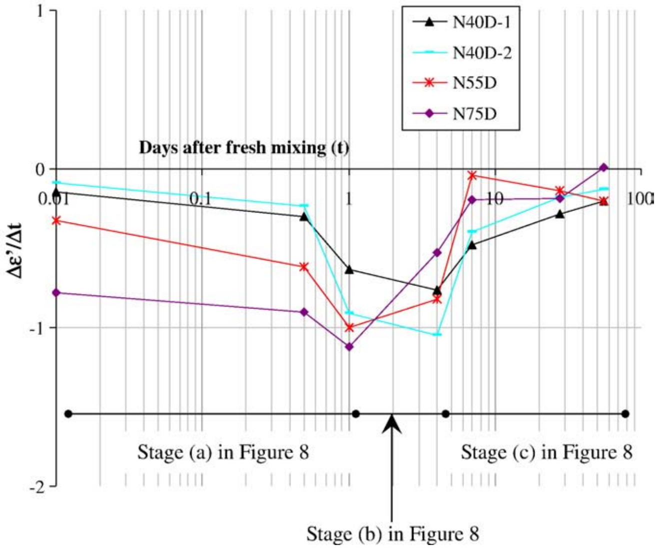

**Fig. 7.** Rate of change of real permittivity for NAC.

### 4.4. Apparent porosity

The apparent porosity (AP) was determined by measuring the weight of vacuum saturated specimens using Eq. (3) [33]. In particular weight $W_d$ was obtained in the short cylindrical specimens (100 mm in diameter and 50 mm long) aged for 28 days. These specimens were oven-dried at 105 °C for 24 h, then put under vacuum at a negative pressure of 0.9 bar for 24 h, and finally saturated with water for 24 h.

$$AP\ (\%) = (W_d - W_o)/(W_d - W_s) \times 100 \tag{3}$$

where $W_d$ = weight of the specimen at 28 days in saturated condition; $W_s$ = weight of the specimen in water under saturated condition; $W_o$ = dry weight of the specimen dried at 105 °C for 24 h.

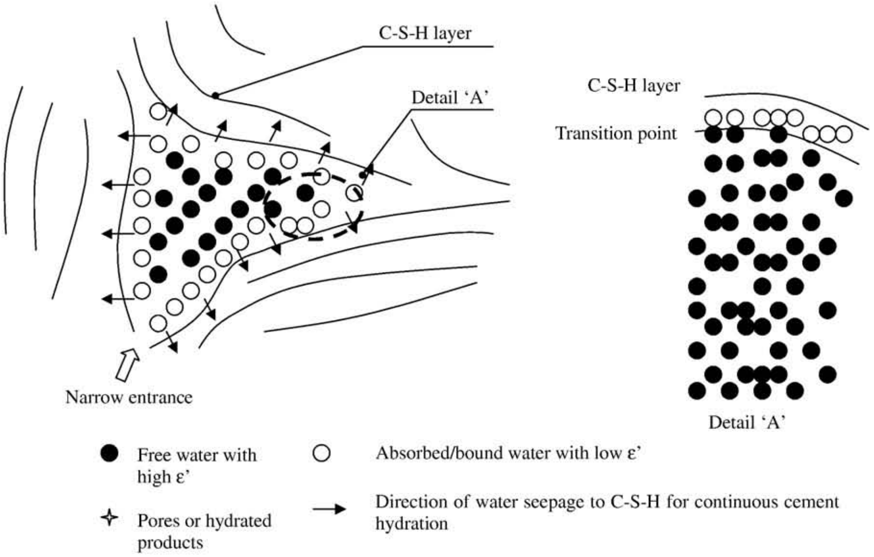

Stage (a) Before transition point in Figures 6 and 7

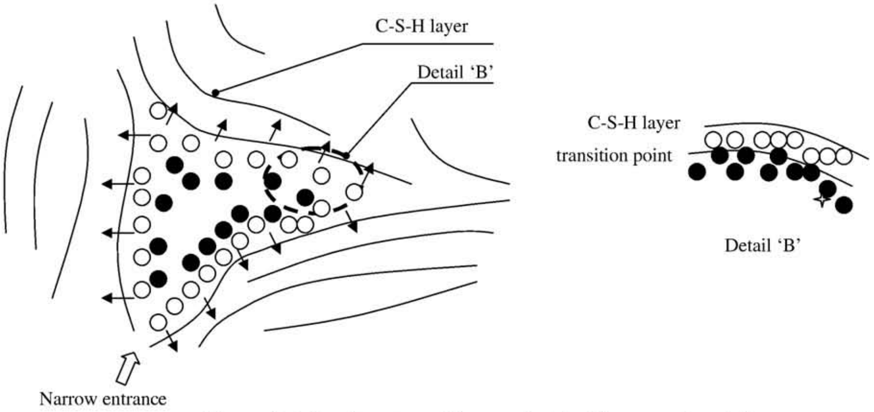

Stage (b) During transition point in Figures 6 and 7

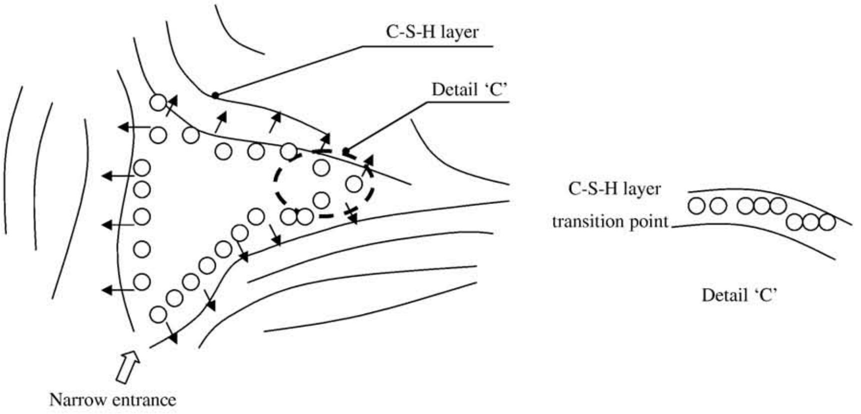

Stage (c) After transition point in Figures 6 and 7

**Fig. 8.** Mechanistic model postulated for cement hydration in LWAC and NAC. Remark: this figure was modified according to [27] and [35].

## 5. Results and discussion

### 5.1. Changes of real permittivity with respect to age

Figs. 4 and 5 show the plots of $\varepsilon'$ and change of $\varepsilon'$ compared to initial value against age ($t$) respectively. The trends in Figs. 4 and 5 were initially steep and became moderate after reaching a transition point for each mix. These changes are apparent in Fig. 6 for LWAC and Fig. 7 for NAC, after differentiating the fitted curves derived from data points shown in Fig. 5. These transition points for LWAC happen at day 7, while those for NAC happen earlier at between day 1 or 4. Despite the limited data available, the physical significance of these transition points can be identified. These points and the associated ages clearly indicate a rapid change of $\varepsilon'$ (free water beyond transition point) and slow change of $\varepsilon'$ (absorbed/bound water within transition point). They represent a process where water went through a critical transition point, in which water molecules continued to be physically absorbed and chemically bounded by the solid particles; rendering other water molecules to further approach the solid particles continuously.

A mechanistic model is formulated in Fig. 8 to generalize the findings depicted in Figs. 4 to 7 and the physical significance discussed above. The model is derived from two well-established systems: capillary pore water system in concrete [34,35] and soil–water system [27]. The model divides the hydration process of cement into three stages:

1. Stage (a): water presents prevalently as free water.
2. Stage (b): at transition point at which free water is less prevalent than before and absorbed/bound water is more prevalent than before.
3. Stage (c): water presents prevalently as absorbed/bound water.

The transition from the free to the absorbed/bound forms of water can be revealed by the transition points observed in Figs. 6 and 7.

### 5.2. Effects of light-weight and normal aggregates on rates of changes of $\varepsilon'$, transition points and porosity

The above section investigated and modeled the similar curve shapes and transition points found in both LWAC and NAC. Further investigations on the curves and transition points allow us to distinguish the unique signatures by LWAC and NAC, from which $\Delta\varepsilon'/\Delta t$ characterizes the process of (1) how much (by the $\Delta\varepsilon'/\Delta t$ axis) and (2) how fast (by the age axis) free water is turned to absorbed/bound water. Two observations are reported as:

(1) according to the variations in the $\Delta\varepsilon'/\Delta t$ axis, LWAC (Fig. 6) exhibited greater rates of changes of $\varepsilon'$ than NAC (Fig. 7) from fresh mix to day 1, and
(2) according to the variations in the age axis, the age associated with the transition points for LWAC (Fig. 6) is approximately day 7, whilst those for NAC (Fig. 7) is much earlier (i.e. approximately from day 1–4).

The first observation is attributed to the fact that porous LWA with high water absorption (reported in Section 3) and large apparent porosity (shown in Fig. 9) possessed much more free water (Table 2) than non-porous natural aggregates. Since free water $\varepsilon'$ is greater than absorbed/bound water $\varepsilon'$, the bleeding process in LWA turned much free water to absorbed/bound water than natural aggregates did within the same period of time. As a result, greater rates of changes of $\varepsilon'$ were found in LWAC. The second observation can be explained by how *fast* free water was being absorbed/bound and turned to absorbed/bound water. In LWAC, this process took longer time as a result of water bleeding from LWA to paste and therefore, the transition was further delayed (day 7) compared to NAC. In NAC, the bleeding process did not exist and so the transition happened much earlier (day 1–4), as shown in Figs. 6 and 7.

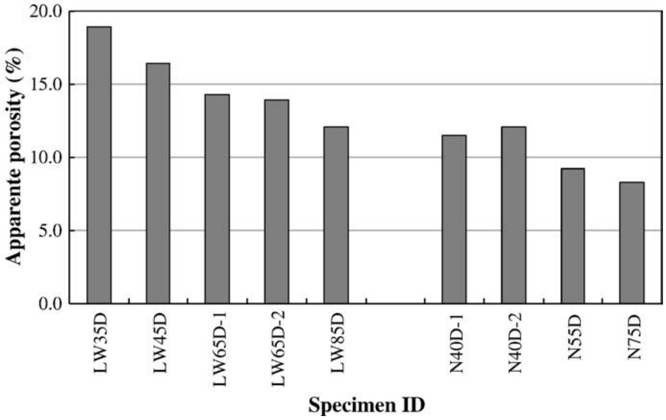

**Fig. 9.** Apparent porosity of LWAC and NAC specimens at age of 28 days.

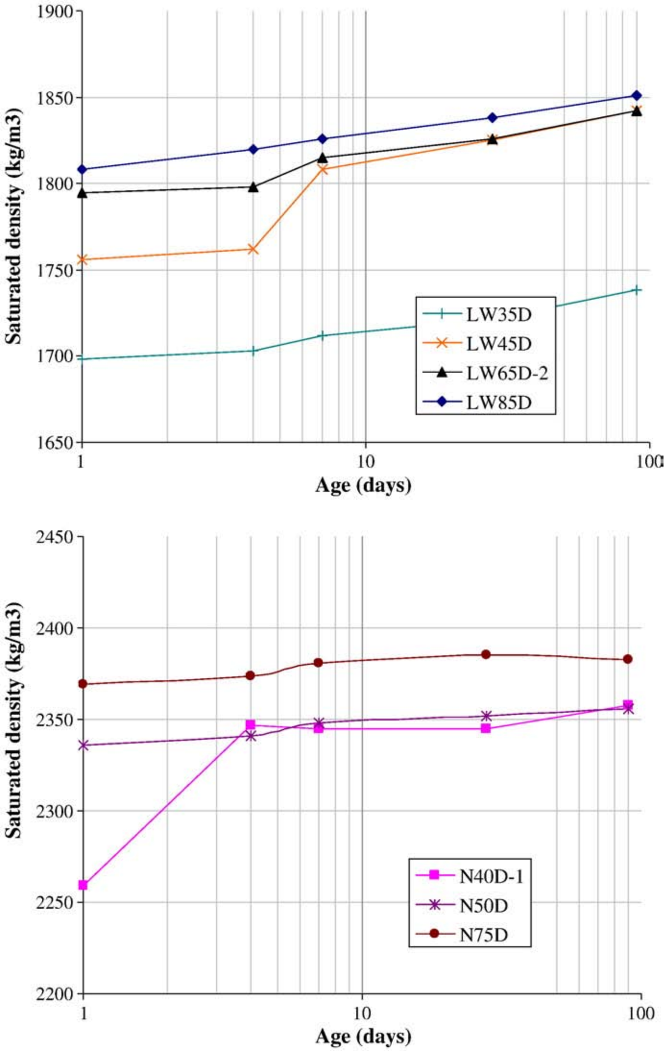

**Fig. 10.** Saturated densities of LWAC (top) and NAC (bottom). Remark: data from L65D-1 and N40D-2 are not measured.

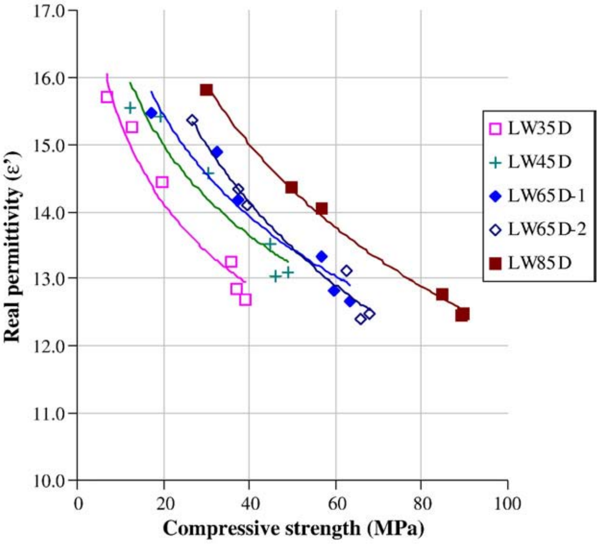

**Fig. 11.** Relationships between real permittivity and compressive strength of LWAC. Remark: the uncertainty of ε' using the 1-GHz GPR is ±0.3.

The LWA bleed water that was present during mixing of LWAC invoked a water migration process from the aggregates to the surrounding cement matrix. Initially the LWA bleed water accumulated within and near the porous aggregates [36]. At later age this LWA bleed water migrated to the cement paste [37,38] because of the reversed saturation gradient across the aggregates and the cement paste. The occurrence of such a mechanism can also be substantiated by data in Fig. 10, where the saturated densities in LWAC continued to increase after 4 days while those of NAC reached a plateau in the meantime. During this time, the porous aggregates in LWAC continuously supplied water to the surrounding cement paste (i.e. bleeding) to form more solid cement hydration product, while this mechanism did not happen in NAC.

### 5.3. Effects of cement hydration on ε', wave energy level and strength

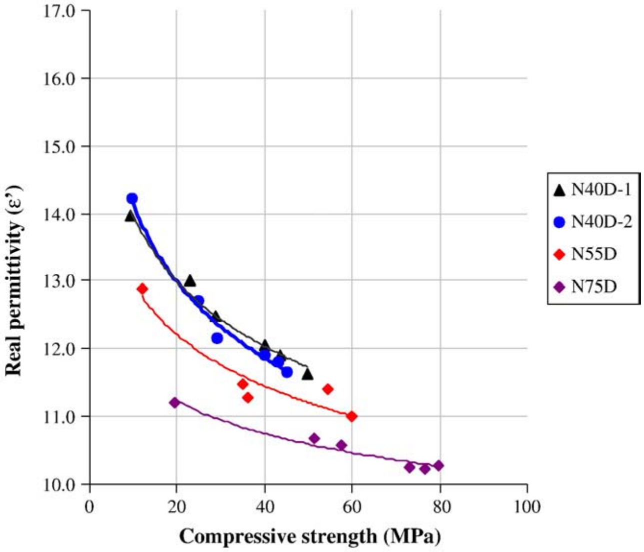

**Fig. 12.** Relationships between real permittivity and compressive strength of NAC specimens. Remark: the uncertainty of ε' using the 1-GHz GPR is ±0.3.

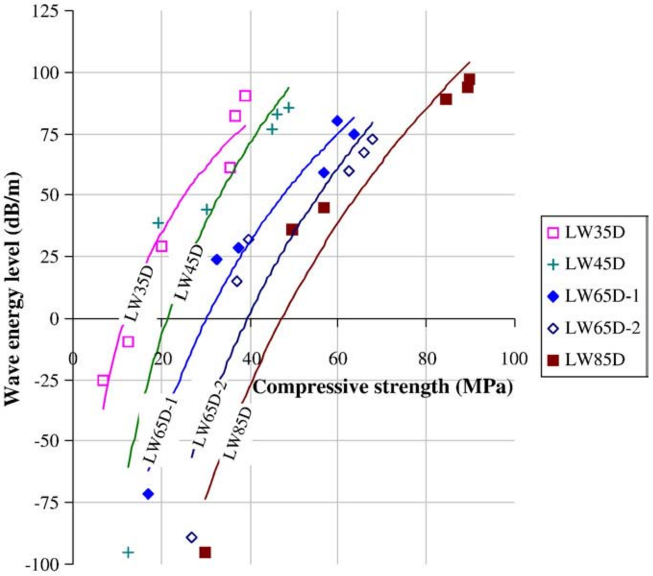

**Fig. 13.** Relationships between wave energy level and compressive strength of LWAC. Remark: the uncertainty of dB/m using the 1-GHz GPR is ±4.

The above mechanism of cement hydration at an early age was arrived at from a dielectric perspective, but can also be understood from the well-known strength perspective. Increase of strength with age relies on building up the C–S–H solid structure geared by the progressive absorption of water which migrates from a free state to an absorbed/bound state, and so on. Figs. 11 and 12 depict the combined relationships of ε' against compressive strength of all specimens at the same age, in which all measured ε' decreased gradually with increasing concrete strength. The reproducibility of the results is demonstrated by the similar results obtained for LW65D-1 and LW65D-2.

These results show that when the concrete specimens were aged and gained higher strength due to cement hydration, their abilities to be polarized by the external EM field were simultaneously reduced. Relationships between wave energy levels against compressive strength are plotted in Figs. 13 and 14. Negative and positive values (computed using Eq. (2)) indicate that the signal amplitudes of the interface at various ages were smaller and greater than the initial amplitude of the ground wave (i.e. $A_{\text{initial}}$ as shown in Fig. 2) respectively. The measured wave energy levels were found to increase with increasing concrete strength and age. This suggests that when the concrete specimens were aged and gained higher strength due to

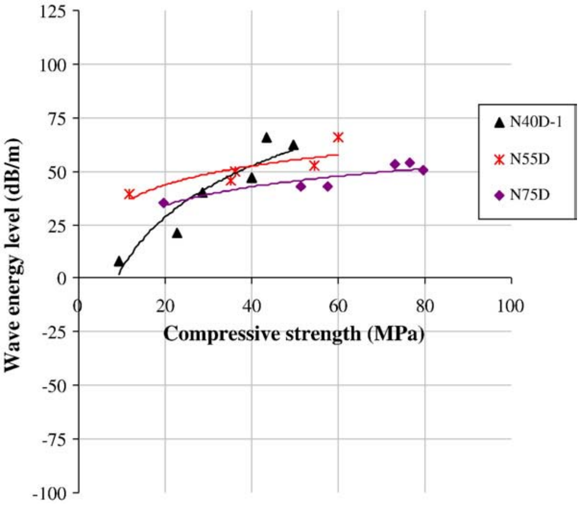

**Fig. 14.** Relationships between wave energy level and compressive strength of NAC specimens. Remarks: the uncertainty of dB/m using the 1-GHz GPR is ±4. Data from N40D-2 are not available.

**Table 3**
Coefficients in formulations between real permittivity vs. strength plotted in Figs. 11 and 12.

| Specimen ID | Coefficient $\alpha$ | Exponent $\beta$ |
|---|---|---|
| LW35D | 20.5 | 0.1247 |
| LW45D | 22.5 | 0.1364 |
| LW65D-1 | 24.7 | 0.1559 |
| LW65D-2 | 31.6 | 0.2192 |
| LW85D | 33.6 | 0.2189 |
| N40D-1 | 17.9 | 0.1074 |
| N40D-2 | 18.8 | 0.1254 |
| N55D | 16.0 | 0.0907 |
| N75D | 13.6 | 0.0646 |

cement hydration, less radar energy was absorbed and as a result, greater magnitudes of reflections from the specimen base were measured. The relationships for both LWAC and NAC are attributed to the continuous cement hydration which have affected both ε' and compressive strength.

The trends reported in Figs. 13 and 14 are attributed to the similar effect of absorbed/bound water and free water on ε' in the concrete. Compared to the young concrete, the smaller amount of free water in the aged concrete absorbed less radar wave energy (measured by wave energy levels), while the strength was developed simultaneously. Similar to ε', this combined effect rendered the ascending trends in Figs. 13 and 14.

For the LWAC that contained silica fume, pozzolanic reaction took place when a sufficient amount of cement was hydrated to give rise to the situation where the pore water was saturated with calcium hydroxide. At this stage calcium silicate hydrate was formed on the surface of the silica fume particles which enhanced the strength development. The second consequence of silica fume is the filling effect which enhanced the packing of the overall concrete matrix and ultimately reduced the porosity at the aggregate–paste interface [35]. However both the pozzolanic reaction and the filling effect of the silica fume did not affect ε' and wave energy levels since neither processes involved free water, especially at the early age of hydration.

The relationships between real permittivity (ε') vs. strength ($f_c$) and wave energy levels ($E$) vs. strength (Tables 3 and 4) were formulated by fitting data according to the best-fit power law and logarithmic regression respectively, as follows:

$$\varepsilon' = \alpha\left(f_c^{-\beta}\right) \tag{4}$$

where $\varepsilon'$ = real permittivity; $f_c$ = strength; $\alpha$ = coefficient and $\beta$ = exponent.

$$E = \gamma \ln(f'_c) - \phi \tag{5}$$

where $E$ = wave energy level (dB/m); $f'_c$ = strength; $\gamma$ and $\phi$ are coefficients.

**Table 4**
Coefficients in formulations between real permittivity vs. strength plotted in Figs. 13 and 14.

| Specimen ID | Coefficient $\gamma$ | Coefficient $\phi$ |
|---|---|---|
| LW35D | 65.9 | 162.9 |
| LW45D | 112.7 | 345.0 |
| LW65D-1 | 109.7 | 374.0 |
| LW65D-2 | 147.0 | 540.5 |
| LW85D | 162.6 | 627.3 |
| N40D-1 | 34.6 | 75.0 |
| N55D | 12.8 | 5.1 |
| N75D | 12.3 | 2.8 |

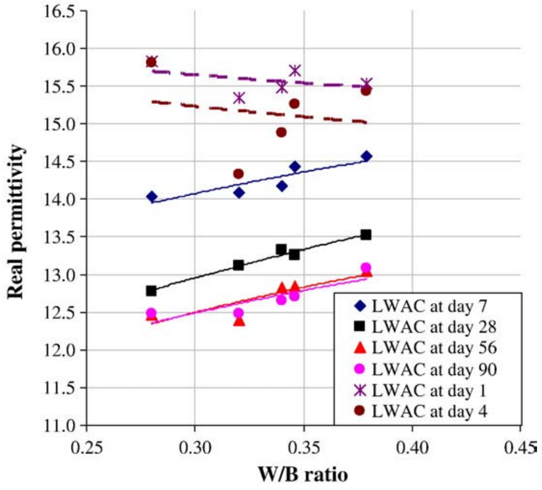

**Fig. 15.** Effects of water to binder ratio on real permittivity measured on LWAC.

### 5.4. Effects of water to binder ratio on ε'

The effects of water to binder ($W/B$) ratio of LWAC and NAC on ε' are plotted in Figs. 15 and 16 respectively. Both figures show the tendency that larger $W/B$ ratio (containing more water) leads to larger ε', except a few fluctuated data reported for LWAC aged 1 and 4 days. This tendency is due to a larger $W/B$ ratio giving rise to higher free water content and therefore larger ε' is resulted. However this explanation does not apply to LWAC aged 1 and 4 days. At these ages and particularly for LWAC only, free water from paste migrated to LWA initially; and this process reversed later, as characterized by radar wave velocity measurement reported in Lai et al., forthcoming. This water-exchange process stopped until day 7 when most free water in LWA was absorbed/bounded, and from this time onward, $W/B$ ratio seemed to influence ε' as plotted in Figs. 15 and 16. The scenario does not happen in NAC because water-exchange process does not occur in NAC in which the aggregates are essentially not porous.

Other factors, such as the total cement content and aggregate content, were commonly known to affect strength. However they do not have any relation with ε' and wave energy levels since these factors neither involve water, nor the mechanism of turning free water to absorbed/bound water during the hydration process.

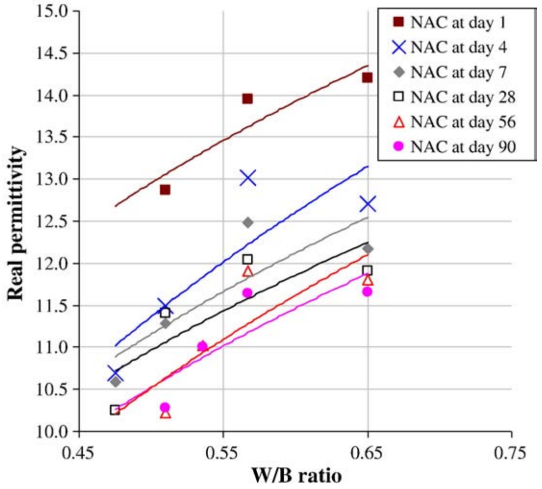

**Fig. 16.** Effect of water to binder ratio on real permittivity measured on NAC.

## 6. Conclusions

The findings of the study are summarized as follows:

1. The mechanism of turning free to absorbed/bound water during the cement hydration process has been described by changes of real permittivity. The results were generalized via a mechanistic model combining the conventional cement hydration and soil–water models.
2. The porous nature and associated bleeding process occurring in LWAC contributed to greater rates of decrease of real permittivity, and delayed transition points compared to NAC.
3. Free water was progressively used up to reduce real permittivity, increase wave energy levels and develop strength for all concretes during cement hydration. This originates from the joint effects of reduced ability to polarize the concretes, progressive development of C–S–H layers and pozzolanic reaction of silica fume.
4. Amongst all factors in mix proportion, only water to binder ratios in both LWAC and NAC were found to influence real permittivity. Other factors in the mixes, such as cement content and inert content do not relate to real permittivity and wave energy levels since factors neither involve water, nor the mechanism of turning free water to absorbed/bound water during the hydration process.

## References

[1] J.H. Bungey, Sub-surface radar testing of concrete: a review, Construction and Building Materials 18 (1) (2004) 1–8.
[2] V.M. Malhotra, N.J. Carino (Eds.), Handbook on Nondestructive Testing of Concrete, 2nd ed., 2006.
[3] H.C. Rhim, Condition monitoring of deteriorating concrete dams using radar, Cement and Concrete Research 31 (3) (2001) 363–373.
[4] Kohl, Streicher, Results of reconstructed and fused NDT-data measured in the laboratory and on-site at bridges, Cement and Concrete Composites 28 (4) (2006) 402–413.
[5] A.P. Annan, Ground Penetrating Radar: Principles, Procedures & Applications, Sensors & Softwares Inc, Mississauga, 2004.
[6] D.J. Daniels (Ed.), Ground Penetrating Radar, 2nd ed., The Institution of Electrical Engineers, London, 2004.
[7] P. Gu, J.J. Beaudoin, Dielectric behaviour of hardened cementitious materials, Advances in Cement Research 9 (33) (1997) 1–8.
[8] W.L. Lai, W.F. Tsang, H. Fang, D. Xiao, Experimental determination of bulk dielectric properties and porosity of porous asphalt and soils using GPR and a cyclic moisture variation technique, Geophysics 71 (4) (2006) K93–K102.
[9] J.A. Huisman, S.S. Hubbard, J.D. Redman, A.P. Annan, Measuring soil water content with ground penetrating radar: a review, Vadose Zone Journal 2 (2003) 476–491.
[10] K. Gorur, M.K. Smit, F.H. Witman, Microwave study of hydrating paste at early age, Cement and Concrete Research 12 (1982) 447.
[11] M.A. Rzepecka, M.A.K. Hamid, A.H. Soliman, Monitoring of concrete curing process by microwave terminal measurements, IEEE Transactions of Industrial Electronics and Control Instrumentation IECI-19 (4) (1972) 120–125.
[12] V.A. Beek, Dielectric properties of young concrete. PhD Thesis, Delft University, 2000.
[13] J.H. Bungey, S.G. Millard, M.R. Shaw, Radar assessment of post-tensioned concrete, 7th International Conference on Structural Faults and Repair, 1997, pp. 331–339.
[14] S. Laurens, J.P. Balayssac, J. Rhazi, G. Arliguie, Influence of concrete relative humidity on the amplitude of ground-penetrating radar (GPR) signal, Materials and Structures 35 (2002) 198–203.
[15] S. Laurens, J.P. Balayssac, J. Rhazi, G. Klysz, G. Arliguie, Non-destructive evaluation of concrete moisture by GPR: experimental study and direct modeling, Materials and Structures 38 (2005) 827–832.
[16] W.L. Lai, W.F. Tsang, Characterization of pore systems of air/water-cured concrete using ground penetrating radar (GPR) through continuous water injection, Construction and Building Materials 25 (3) (2008) 250–256.
[17] W.L. Lai, S.C. Kou, W.F. Tsang, C.S. Poon, Effects of water exchange/bleeding process in early-age light-weight and normal aggregate concrete on radar dielectric measurement, Cement and Concrete Research, under review and forthcoming.
[18] M.D. Knoll, A petrophysical basis for ground-penetrating radar and very early time electromagnetics. Ph.D. Thesis, The University of British Columbia, 1996.
[19] W.L. Lai, Characterization of porous construction materials using electromagnetic radar wave, Ph.D. Thesis, The Hong Kong Polytechnic University, 2006.
[20] M.N. Soutsos, J.H. Bungey, S.G. Millard, M.R. Shaw, A. Patterson, Dielectric properties of concrete and their influence on radar testing, NDT&E International 34 (2001) 419–425.
[21] P. Debye, Polar Molecules, Chemical Publication Company, 1929.
[22] P. Hoekstra, A. Delaney, Dielectric properties of soils at UHF and microwave frequencies, Journal of Geophysical Research 79 (11) (1974) 1699–1708.
[23] Concrete Society, Guidance on radar testing of concrete structures, Concrete Society Technical Report, vol. 48, 1997.
[24] N.R. Peplinski, F.T. Ulaby, M.C. Dobson, Dielectric properties of soils in the 0.3–1.3 GHz range, IEEE Transactions on Geoscience and Remote Sensing 33 (3) (1995) 803–807.
[25] T.J. Marshall, J.W. Holmes, C.W. Rose, Soil Physics, Cambridge University Press, London, 1996.
[26] R. Knight, A. Nur, Geometrical effects in the dielectric response of partially saturated sandstones, The Log Analyst 28 (1987) 513–519.
[27] J.R. Wang, T.J. Schmugge, An empirical model for the complex dielectric permittivity of soils as a function of water content, IEEE Transactions on Geoscience and Remote Sensing GE-18 (4) (1980) 288–295.
[28] R.J. Knight, Hysteresis in the electrical resistivity of partially saturated sandstone, Geophysics 56 (12) (1991) 2139–2147.
[29] BS EN 12620:2002, Aggregates from natural sources for concrete, 2002.
[30] C.A. Balanis, Advanced Engineering Electromagnetics, John Wiley & Sons, New York, NY, 1989 981 pp.
[31] ASTM D6432-99 (Reapproved 2005), Standard guide for using the surface ground penetrating radar method for subsurface investigation, 2005.
[32] BS EN 12504:1 Testing concrete in structures — part 1: cored specimens — taking, examining and testing in compression, 2000.
[33] İ. Türkmen, A. Kantarcı, Effects of expanded perlite aggregate and different curing conditions on the physical and mechanical properties of self-compacting concrete, Building and Environment 42 (6) (2007) 2378–2383.
[34] A.A. Rahman, Characterization of the porosity of hydrated cement paste, in: F.P. Glasserm (Ed.), The Chemistry and Chemically-Related Properties of Concrete, British Ceramic Proceedings, vol. 35, 1984, pp. 249–263.
[35] A.M. Neville, Properties of Concrete, Final ed., Longman, 1995, p. 667.
[36] S.S. Chandra, Lightweight Aggregate Concrete: Science, Technology, and Applications, N.J. Noyes Publications, Norwich, 2003.
[37] C.A. Langton, D.M. Roy, Morphology and microstructure of cement paste/rock interfacial regions, Proc. 7th International Congress on the Chemistry of Cement, Editions Septima, Paris, 1980, pp. 127–132, VIII: VII.
[38] P.K. Mehta, Concrete Structures and Materials, Prentice Hall, NJ, 1986, p. 38.